Interannual variability of air-sea exchange of mercury in the global ocean: the "seesaw effect" in the equatorial Pacific and contributions to the atmosphere

shaojian huang[1] and Yanxu Zhang[1]

[1]Nanjing University

November 24, 2022

Abstract

Air-sea exchange of mercury (Hg) is influenced by meteorological factors that have substantial interannual variability. Here we investigate its interannual variability and influcing factors by using the MITgcm ocean model. We elucidate a latitudinal pattern with a relatively small variability in the mid-latitudes (6.4%-8.5%) and a large one in the Arctic and Equator (15%). Wind speed, salinity, and sea ice dominate the patterns in equatorial, mid-, and high-latitudinal oceans, respectively. A in equatorial Pacific is found between El Niño and La Niña events, owing to wind speed anomaly caused by the variation of Walker circulation. A higher atmospheric Hg concentration (1-2%) in northern hemisphere is found by the GEOS-Chem simulation due to higher ocean evasion fluxes, consistent with the CAMNet and EMEP (1-11%) observations. Besides, a slight fluctuation in the upper tropospheric (±0.5%) reveals a potential contribution from the ocean evasion for interannual variability of tropospheric Hg.

Table S1. Detrended measurement data from CAMNet and EMEP observation sites

Year	Annual Average of Total Hg (ng/m^3)	Annual Average of Total Hg (ng/m^3)
	Ale	**NS**
1994*		
1995	1.63	
1996**	1.57	1.52
1997*	1.55	1.35
1998	1.63	1.30
1999**	1.57	1.64
2000	1.54	1.35
2001	1.63	1.50
2002**	1.58	1.36
2003	1.61	1.49
2004*	1.68	1.51
2005	1.63	1.72
2006	1.62	1.10
2007**	1.57	1.17
2008	1.64	1.35

Year	Annual Average of Total Hg (ng/m^3)	Annual Average of Total Hg (ng/m^3)
2009*	1.53	1.26
2010**		1.34
2011	1.50	
2012	1.43	
2013		
2014	1.60	
2015*	1.66	
2016	1.72	
2017	1.61	
Annual Average	1.59	1.40
Annual Ave of EN years	1.61	1.37
Annual Ave of LN years	1.57	1.41
Difference between LN and EN	2.2%	-2.4%

Note: * and ** represents for El Niño and La Niña years. Blank represents no available data.

Ale: Alert

NS: Nova Scotia

Alb: Alberta

BC: British Columbia

NB: Nouveau-Brunswick

ON: Ontario,

QU: Quebec

SC: Saskat-chewan

MH: Mace Head

Zep: Zeppelin

ZI: Zingst

WD: Waldhof

SC: Schmucke

Interannual variability of air-sea exchange of mercury in the global ocean: the "seesaw effect" in the equatorial Pacific and contributions to the atmosphere

Shaojian Huang[1] and Yanxu Zhang[1*]

[1]School of Atmospheric Sciences, Nanjing University, Nanjing 210023, China

[*]Correspondence to: Yanxu Zhang (zhangyx@nju.edu.cn)

Key Points:

- We spot a latitudinal pattern with a smaller variability in the mid-latitudes (6.4%-8.5%) and a large one in the Arctic and Equator (15%).
- A seesaw pattern in equatorial Pacific is found for evasion flux anomaly (±10%-20%) between El Niño and La Niña events.
- A higher atmospheric Hg (1-2%) in northern hemisphere is simulated due to higher ocean evasion, consistent with the observations (1-11%).

Abstract

Air-sea exchange of mercury (Hg) is influenced by meteorological factors that have substantial interannual variability. Here we investigate its interannual variability and influcing factors by using the MITgcm ocean model. We elucidate a latitudinal pattern with a relatively small variability in the mid-latitudes (6.4%-8.5%) and a large one in the Arctic and Equator (15%). Wind speed, salinity, and sea ice dominate the patterns in equatorial, mid-, and high-latitudinal oceans, respectively. A *seesaw pattern* in equatorial Pacific is found between El Niño and La Niña events, owing to wind speed anomaly caused by the variation of Walker circulation. A higher atmospheric Hg concentration (1-2%) in northern hemisphere is found by the GEOS-Chem simulation due to higher ocean evasion fluxes, consistent with the CAMNet and EMEP (1-11%) observations. Besides, a slight fluctuation in the upper tropospheric (±0.5%) reveals a potential contribution from the ocean evasion for interannual variability of tropospheric Hg.

Plain Language Summary

Mercury is the only metal that is a liquid at room temperature. The strong volatility makes mercury behave like a noble gas in the atmosphere. Like other gases such as CO_2, mercury has an active air-sea exchange, which has an important implication to the biogeochemical cycle of this toxic element. While it is known that the air-sea exchange is the largest term in the global biogeochemical cycle of mercury, the interannual variability and controlling factors remain elusive. We employ a state-of-the-art three-dimensional ocean model to investigate this issue in this study. We find a latitudinal pattern with a relatively small variability in the mid-latitudes and a large one in the Arctic and Equator. A “seesaw pattern” is found in equatorial Pacific between El Niño and La Niña events, owing to the wind speed anomaly caused by the oscillating warming and cooling pattern. Meanwhile, a variability of atmospheric concentration in the northern hemisphere is associated with this pattern. Within the context of climate change and anthropogenic emission controls proposed by the Minamata Convention for Mercury, our work helps to distinguish the natural variability and trend of mercury levels in the environment.

1 Introduction

Mercury (Hg) is a toxic element that is ubiquitous in the environment (Outridge et al., 2018). It comes from both natural (e.g. volcanic eruption) and anthropogenic sources (e.g. fossil fuel combustion, metal mining, and smelting) (Horowitz et al., 2014). Two major chemical forms of Hg exist in the environment: elemental form (Hg^0) that has an atmospheric lifetime of 0.5-1 year and undergoes long-range transport; and divalent form (Hg^{II}) that has a shorter atmospheric lifetime (~1 week) and is deposited near source regions (Selin et al., 2007). Before being buried in deep-sea sediment at the millennium time scale, Hg can be transported and recycled among the global atmosphere, land, and oceans (Outridge et al., 2018). Here, we focus on the air-sea

exchange of Hg^0, which is the largest exchange term between different environmental compartments in global Hg cycle (Horowitcz et al., 2017).

The air-sea exchange of Hg^0 is a bidirectional diffusion process that is driven by the concentration gradients across the atmospheric and seawater interface (Soerensen et al., 2013). The direction of exchange is mainly upward (i.e. evasion from the ocean to the atmosphere) as the Hg^0 in the surface ocean is often supersaturated (Andersson et al., 2008; Mason et al., 2001). The magnitude of Hg^0 exchange flux is influenced by temperature, wave condition, biological film, and turbulence in the atmosphere and ocean surface microlayers, and is typically parameterized as a function of wind speed (Esters et al., 2017). In the marine boundary layer, meteorological conditions such as temperature and wind speed present significantly interannual variability, which is often associated with teleconnections and oscillations of the climate system (Grimm & Natori, 2006; Romero-Centeno et al., 2003). One example is the El Niño-Southern Oscillation (ENSO), characterized as the anomaly in sea surface temperature (SST) through the eastern equatorial Pacific Ocean (Guilderson & Schrag, 1998). The shift of SST would cause the anomalies in sea level pressure and convection, which account for the seasonal and interannual variability of surface wind and rainfall over this region (Janowiak & Arkin, 1991; Wang & Enfield, 2001). In this study, we will examine if the variabilities in meteorological conditions would result in the interannual variability of Hg^0 air-sea exchange fluxes.

The variability in ocean evasion can influence the atmospheric level of Hg^0 as the ocean accounts for more than one-third of the global total Hg sources for the atmosphere (Soerensen et al., 2013). Elevated atmospheric Hg^0 concentrations in an inland site were observed when a springtime noreaster carried the outgassing from the ocean surface (Sigler et al., 2009). Likewise, in coastal stations such as the Mace Head, Ireland and the Cape Point, South Africa, significant interannual variability of gaseous Hg were observed (Ebinghaus et al., 2011; Fisher et al., 2013; Slemr et al., 2008). Slemr et al. (2016) also found an association between the variabilities of Hg concentration and ENSO. Another objective of this study is thus to examine the potential contribution of Hg^0 evasion to the tropospheric Hg^0 levels.

2 Methodology

2.1 MITgcm model

We use the global three-dimensional model MITgcm to stimulate the chemistry and transport of Hg in the global ocean. Details of this model were described in Zhang et al (2019). The model has a horizontal resolution of 1°×1° and 50 vertical levels. The resolution is higher over the Arctic (40 km × 40 km) and the equator (~0.5°×1°) to better represent the ocean currents. Advection and diffusion of Hg are calculated according to the ocean state estimates from the Estimating the Circulation & Climate of the Ocean (ECCO v4) climatology (Forget et al., 2015). The meteorological data that serve as the upper boundary layer of the ocean (e.g. wind speed, air temperature,

precipitation, short-wave and long-wave radiation) are from the ERA-Interim re-analysis fields spanning 1992-2017 (Dee et al., 2011). The air-sea exchange flux of Hg^0 is calculated as follow (Andersson et al., 2008; Fu et al., 2010; Wanninkhof, 1992):

$$F = K_w\left(DGM - GEM/H(T)\right) \quad (1)$$

where F represents the air-sea exchange flux (ng m^{-2} h^{-1}); K_w is the gas exchange velocity (aka piston velocity, cm h^{-1}); GEM represents the gaseous elemental Hg^0 (ng m^{-3}) in the atmosphere; and DGM is the dissolved gaseous Hg^0 in seawater. H(T) is the dimensionless partitioning coefficient for Hg^0 between the atmosphere and seawater. The parametrization of K_w follows Soerensen et al (2010) and Nightingale et al (2000):

$$K_W = 0.31u_{10}^2\left(Sc_{Hg}/Sc_{CO2}\right)^{-0.5} \quad (2)$$

where Sc_{Hg} and Sc_{CO2} are Schmidt numbers of Hg^0 and CO_2, respectively. Henry's law coefficient for Hg^0 is from Andersson (2008):

$$H(T) = exp(-2403.3/T + 6.92) \quad (3)$$

where T is the seawater temperature.

The atmospheric deposition flux of Hg^{II} and Hg^0 concentrations in the marine boundary layer are from the GEOS-Chem model (Zhang et al., 2019). The model is run for 1992-2016 with initial conditions from previous model output (Zhang et al., 2020) and the first two years are discarded as spin-up time.

2.2 GEOS-Chem model

We use the GEOS-Chem model (version v 12.2.1) (www.geos-chem.org) to simulate the impact of Hg^0 evasion flux on the atmospheric levels of Hg. The detail of the model is described by Horowitz et al (2017). This model is driven by assimilated meteorological data archived from the Goddard Earth Observing System (GEOS) of the NASA Global Modeling and Data Assimilation Office (GMAO), with a horizontal resolution of 4° latitude by 5° longitude and 47 vertical eta levels. Three atmospheric Hg tracers including elemental mercury (Hg^0), divalent mercury (Hg^{II}), and particulate mercury (Hg^P) are simulated in this model. The model contains the oxidation of Hg^0 by Br atom and the in-cloud reduction of Hg^{II}. The partitioning between Hg^{II} and Hg^P is modeled following Amos et al. (2012). The model also includes wet deposition of Hg^{II} and Hg^P and dry deposition of all three species. The model is driven by the anthropogenic emission inventory of Hg developed by Zhang et al. (2016). The model also considers natural emissions and re-emissions from soil and snow (Selin et al., 2008). The re-emissions of Hg^0 from the ocean are specified as a constant model input, which is from the output of the MITgcm model. We use the ocean evasion fluxes during different phases of the ENSO cycle, and the differences

of the resulted atmospheric Hg^0 concentrations are calculated. The model is run for five years for each ocean evasion scenario, and the results of the last three years are analyzed.

2.3 Observation datasets

Atmospheric Hg concentration data used in this study are from Canadian Atmospheric Mercury Network (CAMNet), and European Monitoring and Evaluation Program (EMEP) networks. These observation data are used for verifying the calculated trends of our simulations.

Decreasing trends are spotted for the original time series of annual Hg concentration in different observation sites (Zhang et al., 2016). We conduct a linear regression for the atmospheric Hg^0 (or total gaseous Hg, TGM) concentrations with time as an independent variable. The calculated slope is tested by a parametric t-test for significance (α= 0.05) (Xu et al., 2006). If significant, the decreasing trends are removed from the time series by adding the product of slope and time increment.

3 Result and Discussion

3.1 Variability of Hg^0 evasions

Globally, the Hg^0 evasion flux varies between 18.7-19.4 Mmol/y during 1994-2016. A distinct latitudinal pattern emerges for the interannual variability of Hg^0 evasion flux in the global oceans (**Fig. 1, S1-4**). The model indicates that the interannual variability of Hg^0 evasion is relatively small in the mid-latitudes. The relative ranges [defined as (maximum-minimum)/mean] of annual evasion flux are 6.4% and 7.0% in the northern and southern mid-latitude oceans, respectively, and 8.5% for the Southern Ocean. The interannual variability is high over the Arctic Ocean (±10%), which has been mentioned by Fisher et al. (2013). However, a more pronounced fluctuation is simulated for the equatorial regions with a relative range of 15%, with higher variability for the equatorial Pacific (20%) and Atlantic (22%) Oceans than the equatorial Indian Ocean (9.6%) (**Fig. S3**).

Substantial seasonal variability exists for Hg^0 evasion fluxes as noted by previous studies (Soerensen et al., 2010; Song et al., 2015; Strode et al., 2007). The highest Hg^0 evasions are simulated in fall and the lowest in spring in the mid- and high-latitude oceans in both hemispheres (Fig.1 f-g, i-j), reflecting the seasonal cycle of the precipitation, which influences the amount of atmospheric Hg deposition and subsequently the size of the available pool for Hg^0 evasion from the surface ocean. The seasonal cycle of ocean mixed layer depth also reinforces this pattern. Entrainment starting in spring brings up Hg-rich waters from the subsurface ocean, and detrainment in fall decreases the amount of Hg in the mixed layer (Soerensen et al. 2010). In polar regions, the evasion fluxes are the highest in the summertime due to the highest temperature and least ice coverage. The seasonal variation of evasion in

the tropical oceans are more complex with the highest evasion in boreal winter resulting from the strongest wind speed and elevated flux in boreal summer due to larger precipitation in the intertropical convergence zone (Zhang et al., 2019).

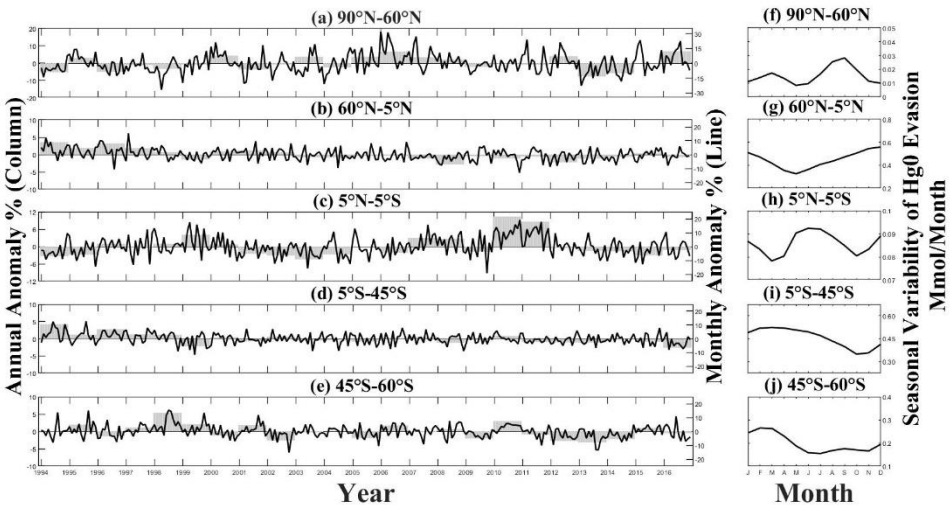

Figure 1. Monthly and annual anomaly (a-e) and monthly mean (f-j) of Hg^0 evasion fluxes in the Arctic, northern temperate, equator, southern temperate, and the Southern Ocean.

3.2 Influencing Factors

Table 1 shows the influence of meteorological parameters (including wind speed, precipitation, air temperature, sea ice fraction, seawater temperature, and salinity) on the annual mean Hg^0 evasion fluxes during 1994-2016. Wind speed is the dominant factor in controlling the interannual variability of Hg^0 evasion in equatorial oceans, except for equatorial Atlantic. For example, Hg^0 evasion has a positive anomaly in 2010 (+8.8%) and 2011 (+5.4%), consistent with the positive anomaly of wind speed (+8.9% and +5.6%, respectively). Inversely, a negative anomaly of Hg^0 evasion (-3.6%) is found in 2015, while the anomaly of wind speed in that year is -6.2% (**Fig. S5**). The correlation coefficients with wind speed are 0.76, 0.55, and 0.21 in the equatorial Pacific, Indian, and Atlantic Oceans, respectively. The correlation between annual Hg^0 evasion and precipitation amount is rather weak, even though a significant correlation relationship was found on a daily time scale (Zhang et al., 2019). The air temperature also has a limited impact on evasion due to the relatively high values as well as little relative variability in the equatorial regions.

Table 1. Correlation between annual Hg^0 evasion fluxes and meteorological parameters in different ocean regions.

Factors		T	Prec.	Wind	SST	S	Sea Ice
Pacific	N	0.02	-0.33	-0.29	0.52**	-0.44*	-
	Eq.	-0.63**	-0.26	0.76**	-0.65**	0.21	-
	S	-0.15	0.10	-0.02	-0.21	-0.07	-

Indian	N	0.03	-0.04	0.17	-0.17	-0.36*	-
	Eq.	0.43*	-0.12	0.59**	0.24	-0.18	-
	S	-0.41*	-0.02	-0.17	-0.43**	-0.23	-
Atlantic	N	-0.57**	-0.02	-0.26	0.26	0.85**	-
	Eq	-0.03	-0.42**	0.21	-0.03	0.06	-
	S	-0.17	0.09	-0.09	-0.30	-0.75**	-
Southern Ocean		0.34	0.11	0.17	-0.19	-0.04	-
Arctic		0.10	0.04	0.01	0.44*	-0.24	-0.61**

****represents the significant correlation at the level of 0.01 (bilateral); *represents the significant correlation at the level of 0.05 (bilateral).**

We find significant correlations between salinity and Hg^0 evasion flux in the mid-latitudes except for the southern Pacific and the Indian Ocean, reflecting similar influencing factors for water evaporation and Hg^0 evasion. Factors such as higher temperatures and stronger wind speed can accelerate the air-sea exchange of both water and Hg^0. This suggests that ocean salinity could serve as an indicator of the interannual variability of Hg^0 evasion flux.

In the Arctic Ocean, sea ice is the leading driving factor for the interannual variability of Hg^0 evasion **(Fig. S6).** An evident positive anomaly of Hg^0 evasion is spotted in 2016 (+6.91%) with a negative sea ice anomaly (-3.2%). Indeed, the air-sea exchange can be blocked by sea ice thus lower sea ice increases Hg^0 evasion fluxes. Lower sea ice also increases the amount of atmospheric Hg^{II} deposition entering the seawater, which would otherwise stay on top of sea ice. Another controlling factor is the SST, which is anti-correlated with sea ice cover. The SST peaks in 2016 with a positive anomaly of 3.2%, which increases the Henry's Law constant for Hg^0 and promotes Hg^0 evasion (eq. 3).

3.3 Seesaw effect of Hg^0 evasion in Equatorial Pacific

We find the equatorial Pacific Ocean has the largest interannual variability for Hg^0 evasion fluxes in the global ocean (20%). This could be attributed to the close air-sea interactions in this region. Indeed, tremendous heat exchange and SST anomaly occur in this region, which can cause anomalies in wind, temperature, and precipitation (Vimont et al., 2003; Wallace et al., 1989). Variability of the hydrodynamics between eastern and western equatorial pacific is the essential element in developing the ENSO cycle, which could trigger the anomalies of zonal wind stress along the equator (Guilderson & Schrag, 1998; Vimont et al., 2003). The expansion and contraction of warm water in the warm pool of the Pacific Ocean could also largely affect the atmospheric convention (Wang & Enfield, 2001) and contribute to the fluctuation of Hg^0 evasion. With an average periodicity of 3.8 years (Quinn et al., 1987), ENSO is highly likely to influence the interannual variability of Hg^0 evasion in the tropical Pacific Ocean.

Given that the El-Niño and La Niña events often peak in November, December and January (NDJ) (An & Wang, 2001), we contrast the average evasion flux during these three months during El Niño (1997, 2004, 2009, and 2015) and La Niña (1996, 1999,

2007, and 2010) years (Fig. 2). The distributions of Hg^0 evasion fluxes for individual years are shown in **Fig. S7-8**). We find a prominent "seesaw pattern" for the spatial distribution of evasion anomaly between El Niño and La Niña years. During El Niño years, the evasion flux is 15-20% lower over Equatorial Pacific (5°S-5°N, 90°W-170°W) and 5-10% higher over western equatorial Pacific (west of 170°W). The evasion flux is also 15-20% higher over 5-15°N (Fig. 2a). The spatial pattern in La Niña years is exactly opposite to that in El Niño years with a similar magnitude of anomalies (Fig. 2b). The detailed pattern varies slightly among individual years (**Fig.** S7 **and S8**), but the overall patterns hold.

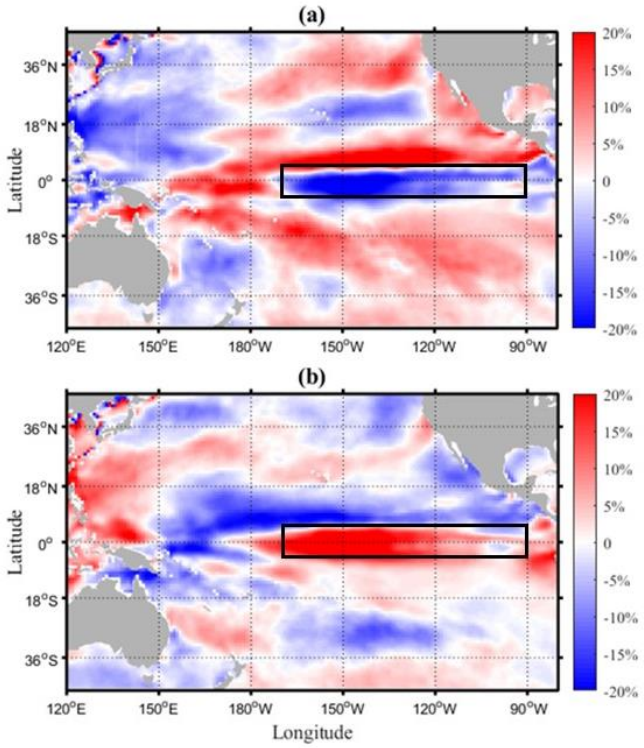

Figure 2. Hg^0 evasion anomaly compared with the average from 1994 to 2016 in November-January (NDJ) of tropical Pacific during El Niño and La Niña years. (a) The average anomaly of all El Niño events and (b) La Niña events. (Black box represents the area within 5°S-5°N, 90°W-170°W)

It is known that the "seesaw pattern" marked the interannual variability of SST anomaly in eastern and western equatorial Pacific related to ENSO (**Fig. S9**). Pronounced "seesaw patterns" are also spotted for the wind speed anomaly during the El Niño and La Niña event (**Fig. S10**). During El Niño years, the wind speed is about 15%-20% lower over Equatorial Pacific (120°W to 150°E), while an exactly opposite spatial pattern is spotted in La Niña years (**Fig. S10a, b**).

Fig. 3 illustrates the connection between the anomaly of Walker circulation and Hg^0 evasion fluxes during El Niño and La Niña events. During the El Niño event, the increase of SST in the central-eastern Pacific Ocean decreases the zonal sea surface temperature gradient, which causes a collapse of the Walker circulation (Cess et al.,

2001). The southeast trades are thus weakened or even reserved, contributing to slower air-sea exchange velocity of Hg^0 (K_w). Meanwhile, the upward atmospheric motion enhances precipitation over the central or eastern Pacific Ocean, which provides more Hg^{II} wet deposition to seawater for evasion (**Fig. 3a**). During the La Niña event, the below-average SST across the east-central Equatorial Pacific Ocean enhances the Walker circulation, resulting in a strong southeast trade wind and Hg^0 evasion velocity. The precipitation is also moved to the western Pacific, causing a positive anomaly of Hg^0 evasion flux there (**Fig. 3b**).

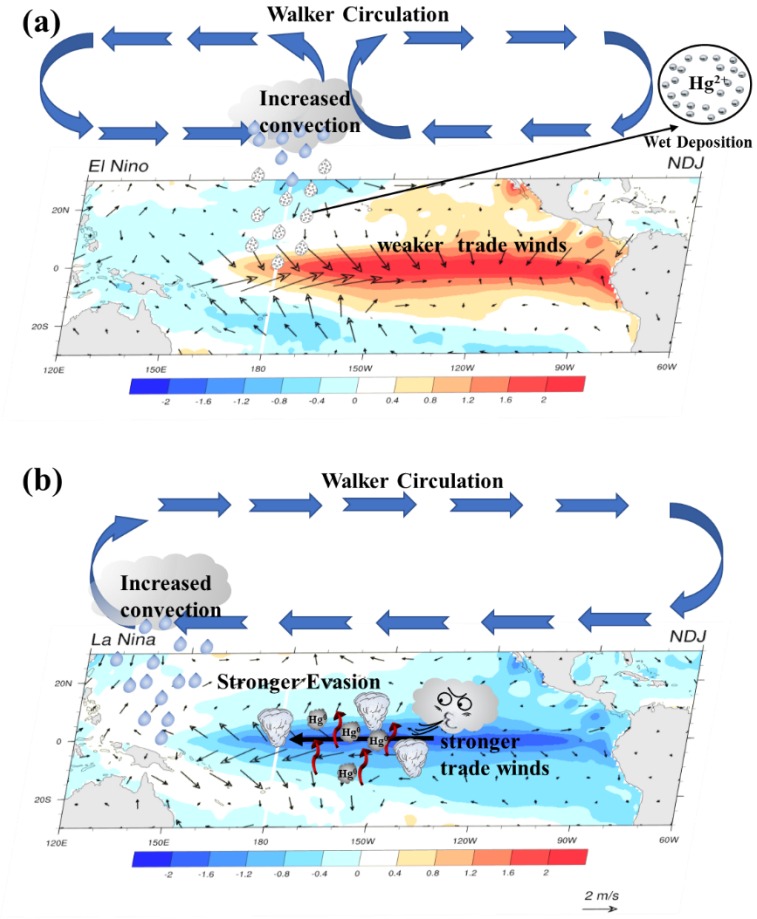

Figure 3. The anomaly of SST and 10 m wind speed in the tropical Pacific Ocean during El Niño (a) and La Niña (b) events and its impact on Hg^0 evasion. (Warm color represents for a positive anomaly of SST while cold color is for a negative anomaly. Arrows present the wind vector).

3.4 Impact of Hg^0 Evasion on Atmospheric Levels

Fig. 4 shows the impact of the variability of Hg^0 evasion on the atmospheric Hg levels (their annual anomalies are available in **Fig. S11 -S12**). Compared to the spatial pattern of Hg^0 evasion anomaly (**Fig. 2**), that of the atmospheric Hg level is generally smoothed due to the relatively long atmospheric lifetime of Hg^0. Globally, higher concentration (1.5 ppq) and deposition (0.06 $ug \cdot m^{-2} \cdot a^{-1}$) of Hg levels are modeled

during La Niña events comparing to El Niño events. The atmospheric Hg levels are reduced in the northern hemisphere during El Niño years as a result of lower evasion fluxes (-0.41%), while the differences in the southern hemisphere are relatively small (+0.23%). Nevertheless, distinct spatial patterns are modeled for these influences with higher Hg levels (10 ppq and 14 $ug \cdot m^{-2} \cdot a^{-1}$) in the equatorial Pacific during El Niño events but with higher THg concentration in the Arctic region during La Niña events (12 ppq). The average evasion flux in the western equatorial Pacific Ocean (5°S-5°N, 130°E-170°W) is 6.2 % higher in El Niño events than in La Niña events, which has caused the variability of atmospheric concentrations and deposition fluxes in this region.

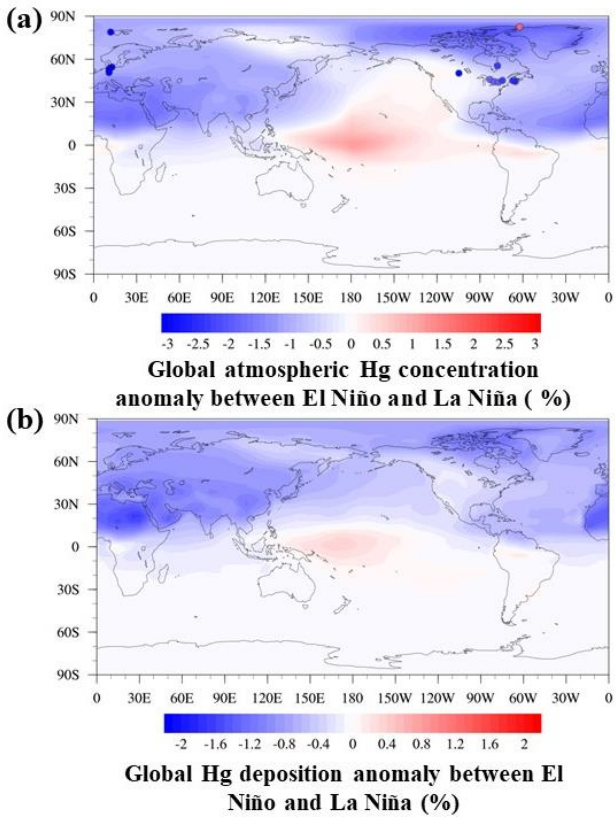

Figure 4. The simulated difference of global a) atmospheric Hg concentrations and b) THg deposition during El Niño and La Niña events by the GEOS-Chem model. Observed differences in atmospheric Hg concentration in North America (CAMNet) and Europe (EMEP) are compared with the simulation and shown as colored dots. The modeled higher atmospheric Hg concentrations over the western equatorial Pacific Ocean over El Niño years are consistent with measurement data. A previous study found short peaks of GEM concentration (1.2-2.5 ng/m^3) on the Gunn Point Peninsula (northern Australia) during November and December of 2015, a strong El Niño event (Howard et al., 2017). While the study attributed the short peaks to biomass burnings, the wind directions during these observations indicated that the air parcel was mainly from the sea surface (**Fig. S10**). Meanwhile, **Fig. 4a** also displays some available surface measurement results from CAMNet and EMEP stations

(Details are displayed in **Table S1**). Generally, there is a similar pattern between our simulation and observation results in both North America and Europe. In Europe, observation sites such as Mace Head and Zepplin reveal a decreasing trend (-1% to -11%) in TGM concentration during El Niño years. Most stations in CAMNet also show a lower TGM concentration in El Niño years (-1.8% to -3.1%) comparing to La Niña years. This agreement suggests a potential contribution from the variability of ocean evasion in these regions, among other factors such as the atmospheric circulation, biomass burning, and anthropogenic emissions.

The measurements at Alert site present an increasing pattern in El Niño years (+2.2%). Based on our simulation, the Hg^0 concentration has a negative anomaly (2 ppq) in the Arctic in El Niño events (**Fig. S11b**). It has been found that Arctic sea ice anomaly can occur along with ENSO, with less sea ice following by a strong La Niña event (Han et al., 2016). The reduced sea ice fraction enhances evasion and subsequently atmospheric TGM concentrations during La Niña events in the Arctic (**Table S1**).

Besides, overall lower Hg deposition fluxes are modeled over north hemispheric terrestrial environment during El Niño years, especially over East Asia (12.8 $ug \cdot m^{-2} \cdot a^{-1}$), South Asia (7.65 $ug \cdot m^{-2} \cdot a^{-1}$), West Europe (9.23 $ug \cdot m^{-2} \cdot a^{-1}$), and Central America (9.97 $ug \cdot m^{-2} \cdot a^{-1}$), which indicates potential less ecological toxic effects in these regions. Available measurement also shows lower deposition fluxes of Hg in the southern Mexico coast in 2004 (an El Niño event) than in 2003 and 2005 (Hansen & Gay, 2013).

Slemr et al. (2016) have also found an interannual variability of tropospheric (10-12 km) Hg concentrations, with a time lag of 8±2 months after El Niño. They also accounted for this variability to biomass burning because of the large uncertainties of estimated Hg emissions from this source. Based on our study, Hg evasion anomaly from sea surface during ENSO is also able to fluctuate the global upper tropospheric Hg concentrations between El Niño and La Niña years in the northern hemisphere, although the trend is relatively weak (±0.5%, **Fig. S13**). Therefore, the Hg evasion anomaly should be a potential contributor to the interannual variability of tropospheric Hg.

Acknowledgments

The authors gratefully acknowledge financial support from National Natural Science Foundation of China (NNSFC) 41875148, Start-up fund of the Thousand Youth Talents Plan, Jiangsu Innovative and Entrepreneurial Talents Plan, and the Collaborative Innovation Center of Climate Change, Jiangsu Province. Meteorological data used in the manuscript are available at **https://apps.ecmwf.int/datasets/data/interim-full-daily/levtype=sfc/**. Atmospheric Hg concentration data are available from CAMNet (**http://donnees.ec.gc.ca/data/**),

and EMEP (**https://www.emep.int/**) networks.

Reference

An, S. I., & Wang, B. (2001). Mechanisms of locking of the El Niño and La Niña mature phases to boreal winter. *Journal of Climate*, *14*(9), 2164–2176. https://doi.org/10.1175/1520-0442(2001)014<2164:MOLOTE>2.0.CO;2

Andersson, M E, Sommar, J., Gårdfeldt, K., & Lindqvist, O. (2008). Enhanced concentrations of dissolved gaseous mercury in the surface waters of the Arctic Ocean. *Marine Chemistry*, *110*(3), 190–194. https://doi.org/https://doi.org/10.1016/j.marchem.2008.04.002

Andersson, Maria E., Gårdfeldt, K., Wängberg, I., & Strömberg, D. (2008). Determination of Henry's law constant for elemental mercury. *Chemosphere*, *73*(4), 587–592. https://doi.org/10.1016/j.chemosphere.2008.05.067

Cess, R. D., Zhang, M., Wang, P. H., & Wielicki, B. A. (2001). Cloud structure anomalies over the tropical Pacific during the 1997/98 El Nino. *Geophysical Research Letters*, *28*(24), 4547–4550. https://doi.org/10.1029/2001GL013750

Dee, D. P., Uppala, S. M., Simmons, A. J., Berrisford, P., Poli, P., Kobayashi, S., et al. (2011). The ERA-Interim reanalysis: Configuration and performance of the data assimilation system. *Quarterly Journal of the Royal Meteorological Society*, *137*(656), 553–597. https://doi.org/10.1002/qj.828

Ebinghaus, R., Jennings, S. G., Kock, H. H., Derwent, R. G., Manning, A. J., & Spain, T. G. (2011). Decreasing trends in total gaseous mercury observations in baseline air at Mace Head, Ireland from 1996 to 2009. *Atmospheric Environment*, *45*(20), 3475–3480. https://doi.org/10.1016/j.atmosenv.2011.01.033

Esters, L., Landwehr, S., Sutherland, G., Bell, T. G., Christensen, K. H., Saltzman, E. S., et al. (2017). Parameterizing air-sea gas transfer velocity with dissipation. *Journal of Geophysical Research: Oceans*, *122*(4), 3041–3056. https://doi.org/10.1002/2016JC012088

Fisher, J. A., Jacob, D. J., Soerensen, A. L., Amos, H. M., Corbitt, E. S., Streets, D. G., et al. (2013). Factors driving mercury variability in the Arctic atmosphere and ocean over the past 30 years. *Global Biogeochemical Cycles*, *27*(4), 1226–1235. https://doi.org/10.1002/2013GB004689

Forget, G., Campin, J.-M., Heimbach, P., Hill, C. N., Ponte, R. M., & Wunsch, C. (2015). ECCO version 4: an integrated framework for non-linear inverse modeling and global ocean state estimation. *Geosci. Model Dev.*, *8*(10), 3071–3104.

https://doi.org/10.5194/gmd-8-3071-2015

Fu, X., Feng, X., Zhang, G., Xu, W., Li, X., Yao, H., et al. (2010). Mercury in the marine boundary layer and seawater of the South China Sea: Concentrations, sea/air flux, and implication for land outflow. *Journal of Geophysical Research Atmospheres*, *115*(6), 1–11. https://doi.org/10.1029/2009JD012958

Grimm, A. M., & Natori, A. A. (2006). Climate change and interannual variability of precipitation in South America. *Geophysical Research Letters*, *33*(19), 1–5. https://doi.org/10.1029/2006GL026821

Guilderson, T. P., & Schrag, D. P. (1998). Abrupt shift in subsurface temperatures in the tropical Pacific associated with changes in El Nino. *Science*, *281*(5374), 240–243. https://doi.org/10.1126/science.281.5374.240

Han, Z., Li, S., Liu, J., Gao, Y., & Zhao, P. (2016). Linear Additive Impacts of Arctic Sea Ice Reduction and La Niña on the Northern Hemisphere Winter Climate. *Journal of Climate*, *29*(15), 5513–5532. https://doi.org/10.1175/JCLI-D-15-0416.1

Hansen, A. M., & Gay, D. A. (2013). Observations of mercury wet deposition in Mexico. *Environmental Science and Pollution Research*, *20*(12), 8316–8325. https://doi.org/10.1007/s11356-013-2012-3

Horowitz, H. M., Jacob, D. J., Amos, H. M., Streets, D. G., & Sunderland, E. M. (2014). Historical Mercury Releases from Commercial Products: Global Environmental Implications. *Environmental Science & Technology*, *48*(17), 10242–10250. https://doi.org/10.1021/es501337j

Horowitz, H. M., Jacob, D. J., Zhang, Y., Dibble, T. S., Slemr, F., Amos, H. M., et al. (2017). A new mechanism for atmospheric mercury redox chemistry: implications for the global mercury budget. *Atmospheric Chemistry and Physics*, *17*(10). https://doi.org/10.5194/acp-17-6353-2017

Howard, D., Nelson, P. F., Edwards, G. C., Morrison, A. L., Fisher, J. A., Ward, J., et al. (2017). Atmospheric mercury in the Southern Hemisphere tropics: Seasonal and diurnal variations and influence of inter-hemispheric transport. *Atmospheric Chemistry and Physics*, *17*(18), 11623–11636. https://doi.org/10.5194/acp-17-11623-2017

Janowiak, J. E., & Arkin, P. A. (1991). Rainfall variations in the tropics during 1986-1989, as estimated from observations of cloud-top temperature. *Journal of Geophysical Research*, *96*(D Suppl.), 3359–3373. https://doi.org/10.1029/90jd01856

Mason, R. P., Lawson, N. M., & Sheu, G.-R. (2001). Mercury in the Atlantic Ocean: factors controlling air–sea exchange of mercury and its distribution in the upper

waters. *Deep Sea Research Part II: Topical Studies in Oceanography*, *48*(13), 2829–2853. https://doi.org/10.1016/S0967-0645(01)00020-0

Nightingale, P. D., Malin, G., Law, C. S., Watson, A. J., Liss, P. S., Liddicoat, M. I., et al. (2000). In situ evaluation of air-sea gas exchange parameterizations using novel conservative and volatile tracers. *Global Biogeochemical Cycles*, *14*(1), 373–387. https://doi.org/10.1029/1999GB900091

Outridge, P. M., Mason, R. P., Wang, F., Guerrero, S., & Heimbürger-Boavida, L. E. (2018). Updated Global and Oceanic Mercury Budgets for the United Nations Global Mercury Assessment 2018. *Environmental Science & Technology*, *52*(20), 11466–11477. https://doi.org/10.1021/acs.est.8b01246

Quinn, W. H., Neal, V. T., & Antunez De Mayolo, S. E. (1987). El Niño occurrences over the past four and a half centuries. *Journal of Geophysical Research: Oceans*, *92*(C13), 14449–14461. https://doi.org/10.1029/JC092iC13p14449

Romero-Centeno, R., Zavala-Hidalgo, J., Gallegos, A., & O'Brien, J. J. (2003). Isthmus of tehuantepec wind climatology and ENSO signal. *Journal of Climate*, *16*(15), 2628–2639. https://doi.org/10.1175/1520-0442(2003)016<2628:IOTWCA>2.0.CO;2

Selin, N. E., Jacob, D. J., Yantosca, R. M., Strode, S., Jaeglé, L., and Sunderland, E. M. (2008), Global 3-D land-ocean-atmosphere model for mercury: Present-day versus preindustrial cycles and anthropogenic enrichment factors for deposition, Global Biogeochem. Cycles, 22, GB2011, doi:10.1029/2007GB003040.

Selin, N. E., Jacob, D. J., Park, R. J., Yantosca, R. M., Strode, S., Jaeglé, L., and Jaffe, D. (2007), Chemical cycling and deposition of atmospheric mercury: Global constraints from observations, J. Geophys. Res., 112, D02308, doi:10.1029/2006JD007450.

Sigler, J. M., Mao, H., & Talbot, R. (2009). Gaseous elemental and reactive mercury in Southern New Hampshire. *Atmos. Chem. Phys.*, *9*(6), 1929–1942. https://doi.org/10.5194/acp-9-1929-2009

Slemr, F., Brunke, E. G., Labuschagne, C., & Ebinghaus, R. (2008). Total gaseous mercury concentrations at the Cape Point GAW station and their seasonality. *Geophysical Research Letters*, *35*(11), 1–5. https://doi.org/10.1029/2008GL033741

Slemr, Franz, Brenninkmeijer, C. A., Rauthe-Schöch, A., Weigelt, A., Ebinghaus, R., Brunke, E. G., et al. (2016). El Niño-Southern Oscillation influence on tropospheric mercury concentrations. *Geophysical Research Letters*, *43*(4), 1766–1771. https://doi.org/10.1002/2016GL067949

Soerensen, A. L., Sunderland, E. M., Holmes, C. D., Jacob, D. J., Yantosca, R. M.,

Skov, H., et al. (2010). An improved global model for air-sea exchange of mercury: High concentrations over the North Atlantic. *Environmental Science and Technology*, *44*(22), 8574–8580. https://doi.org/10.1021/es102032g

Soerensen, A. L., Mason, R. P., Balcom, P. H., & Sunderland, E. M. (2013). Drivers of surface ocean mercury concentrations and air-sea exchange in the West Atlantic Ocean. *Environmental Science and Technology*, *47*(14), 7757–7765. https://doi.org/10.1021/es401354q

Song, S., Selin, N. E., Soerensen, A. L., Angot, H., Artz, R., Brooks, S., et al. (2015). Top-down constraints on atmospheric mercury emissions and implications for global biogeochemical cycling. *Atmos. Chem. Phys.*, *15*(12), 7103–7125. https://doi.org/10.5194/acp-15-7103-2015

Strode, S. A., Jaeglé, L., Selin, N. E., Jacob, D. J., Park, R. J., Yantosca, R. M., et al. (2007). Air-sea exchange in the global mercury cycle. *Global Biogeochemical Cycles*, *21*(1), 1–12. https://doi.org/10.1029/2006GB002766

Vimont, D. J., Wallace, J. M., & Battisti, D. S. (2003). The seasonal footprinting mechanism in the Pacific: Implications for ENSO. *Journal of Climate*, *16*(16), 2668–2675. https://doi.org/10.1175/1520-0442(2003)016<2668:TSFMIT>2.0.CO;2

Wallace, J. M., Mitchell, T. P., & Deser, C. (1989). The Influence of Sea-Surface Temperature on Surface Wind in the Eastern Equatorial Pacific: Seasonal and Interannual Variability. *Journal of Climate*, *2*(12), 1492–1499. https://doi.org/10.1175/1520-0442(1989)002<1492:TIOSST>2.0.CO;2

Wang, C., & Enfield, D. B. (2001). The tropical western hemisphere warm pool. *Geophysical Research Letters*, *28*(8), 1635–1638. https://doi.org/10.1029/2000GL011763

Wanninkhof, R. (1992). Relationship between wind speed and gas exchange over the ocean. *Journal of Geophysical Research*, *97*(C5), 7373–7382. https://doi.org/10.1029/92JC00188

Xu, C., Gong, L., Jiang, T., Chen, D., & Singh, V. P. (2006). Analysis of spatial distribution and temporal trend of reference evapotranspiration and pan evaporation in Changjiang (Yangtze River) catchment. *Journal of Hydrology*, *327*(1), 81–93. https://doi.org/10.1016/j.jhydrol.2005.11.029

Zhang, Y., Jacob, D. J., Horowitz, H. M., Chen, L., Amos, H. M., Krabbenhoft, D. P., et al. (2016). Observed decrease in atmospheric mercury explained by global decline in anthropogenic emissions. *Proceedings of the National Academy of Sciences*, 201516312. https://doi.org/10.1073/pnas.1516312113

Zhang, Y., Horowitz, H., Wang, J., Xie, Z., Kuss, J., & Soerensen, A. L. (2019). A

Coupled Global Atmosphere-Ocean Model for Air-Sea Exchange of Mercury: Insights into Wet Deposition and Atmospheric Redox Chemistry. *Environmental Science and Technology*, *53*(9), 5052–5061. https://doi.org/10.1021/acs.est.8b06205

Zhang, Y., Soerensen, A. L., Schartup, A. T., & Sunderland, E. M. (2020). A Global Model for Methylmercury Formation and Uptake at the Base of Marine Food Webs. *Global Biogeochemical Cycles*, *34*(2), e2019GB006348. https://doi.org/10.1029/2019GB006348